Extensional deformation of non-Newtonian liquid bridges

S. Gaudet, G. H. McKinley

Abstract A numerical method for simulating the extensional dynamics of elongating filaments of non-Newtonian fluids in a filament stretching rheometer is presented. The boundary element method, in conjunction with either the Oldroyd-B or the generalized multimode Upper-Convected Maxwell constitutive model, is used to calculate the transient evolution of the liquid interface, the applied force on the stationary end plate and the polymeric stresses. The numerical results are compared to experimental results and are in excellent agreement at low Hencky strains (Newtonian response) but provide less accurate modeling of the stress growth observed in experiments at higher strains. A comparison of different methods for measuring the apparent extensional viscosity from global measurements of the net force and the mid-point radius of the filament is presented. At large strains calculations show that the fluid motion in these devices closely approximates ideal uniaxial elongation.

1
Introduction

The characterization of a fluid's response to elongational deformation is of importance because of the wide variety of flows with dominant extensional kinematics that arise in industrial processes. Fiber-spinning, extrusion and injection molding are examples of processes in which many types of non-Newtonian liquids undergo significant elongational stretching. Many of these fluids are viscoelastic and do not exhibit a resistance to elongation proportional

S. Gaudet
Department of Mathematics and Statistics,
Université de Moncton, Moncton,
New Brunswick, Canada, E1A 3E9

G. H. McKinley
Division of Engineering and Applied Sciences,
Harvard University, Cambridge, MA 02138, USA

Correspondence to: S. Gaudet

to the rate at which they are being extended, as is the case for Newtonian fluids. In fact, the extensional viscosity of viscoelastic fluids, such as polymer solutions, can increase dramatically, and in a nonlinear manner, with strain and with the rate of deformation. Although rheometric methods for measuring the extensional viscosity of high-viscosity, rigid fluids such as polymer melts (Meissner (1985a, 1985b)) are well established, methods for determining the extensional properties of more mobile complex fluids such as polymer solutions are still being developed (Khagram, Gupta and Sridhar (1985); Gupta and Sridhar (1988); James and Walters (1993); Hermanksy and Boger (1995)). Ferguson and Hudson (1993) showed the dramatic discrepancies that can arise in the measurements of the extensional viscosity of a single test fluid when different experimental test configurations are used. These difficulties in measuring extensional properties frequently arise due to the presence of shearing effects near solid surfaces (Gupta and Sridhar (1988); James and Walters (1993)) which significantly affect experimentally measured quantities such as the pressure drop or tensile force.

The velocity components in an ideal homogeneous uniaxial extensional flow are

$$u_r = -\tfrac{1}{2}\dot{\varepsilon}r, \quad u_z = \dot{\varepsilon}z, \quad u_\theta = 0 \; , \tag{1}$$

where u_r, u_z and u_θ are the radial, axial and azimuthal velocities, respectively and $\dot{\varepsilon}$ is the (constant) extension rate. For this flow field an extensional viscosity can be defined as

$$\bar{\eta} = \frac{T_{zz} - T_{rr}}{\dot{\varepsilon}} \; , \tag{2}$$

where T_{zz} and T_{rr} are, respectively, the axial and radial normal stresses in the fluid. An ideal extensional rheometer would be one that reproduces a shear-free flow field similar to (1) while measuring the stress difference $T_{zz} - T_{rr}$ at a point. However in practice, the inherent difficulty in realizing an ideal shear-free extensional flow such as (1) is that shearing effects are always introduced when a fluid sample is physically elongated; primarily due to the presence of no-slip boundary conditions at solid surfaces which introduce vorticity. These kinematic difficulties have been discussed in detail in James and Walters (1993) and numerical computations can play an important role in guiding design of experimental protocols that minimize these undesired nonhomogeneities.

The filament (or liquid bridge) stretching apparatus illustrated in Fig. 1 is a device that attempts to reproduce the flow field in (1) and is the experimental configuration
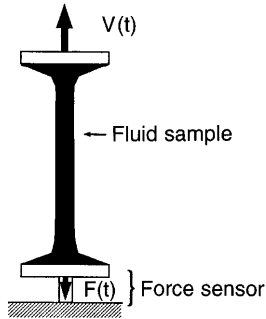
V(t)

← Fluid sample

F(t) } Force sensor

Fig. 1. Fluid filament stretching device

which has arguably yielded the most consistent extensional viscosity measurements for polymer solutions thus far. Sridhar, Tirtaatmadja, Nguyen and Gupta (1991) and Tirtaatmadja and Sridhar (1993) were the first to present extensional viscosity measurements using this apparatus. Since then several similar experimental devices have been used by different investigators (see the recent work by Spiegelberg, Ables and McKinley (1996) for a review). However, the liquid bridge stretching device does not generate a uniform shear-free flow. Shearing effects are present in the flow near the end plates because of the pinning of fluid elements adjacent to the solid end-plate fixtures. Furthermore, the flow is spatially non-homogeneous since different strain rates are experienced at different locations in the liquid sample. Velocity compensation techniques (Tirtaatmadja and Sridhar (1993); Spiegelberg, Ables and McKinley (1996)) are used in experiments in order to generate local regions of uniform strain rates within the fluid filament in an attempt to simplify calculations of the extensional viscosity of the test sample.

Despite all the recent experimental attention, numerical simulations of extensional rheometers, such as the one in Fig. 1, are scarce. Shipman, Denn and Keunings (1991) presented a numerical study of viscoelastic fluid samples described by the Oldroyd-B model undergoing extensional stretching in an attempt to simulate the low-rate experiments of Sridhar, Tirtaatmadja, Nguyen and Gupta (1991). As a result of numerical difficulties only parts of the liquid filament near the rigid end plates were simulated and an approximate initial surface configuration was selected. Viscoelastic fluids have a fading memory of their previous deformations and as shown by Spiegelberg, Ables and McKinley (1996) the initial configuration of the fluid in a filament stretching device can play an important role in defining the evolution of the transient uniaxial extensional stresses in the filament at large strains. Extensional deformations of Newtonian liquid bridges at large strains were studied numerically by Gaudet, McKinley and Stone (1996) who used the boundary element method to study the effects of interfacial tension, outer fluid viscosity and the initial bridge configuration on the dynamics of these viscously dominated, quasi-steady flows. Although the total force required to elongate the fluid filaments was calculated in this study, no attention was given to the calculation of the extensional viscosity.

An integral equation representation of the momentum equation for flows involving non-Newtonian fluids (Bush (1984)) can also be developed using the boundary element method, but the more complicated constitutive relationships require treatment of volume integrals in the numerical implementation. Bush, Milthorpe and Tanner (1984) and Bush, Tanner and Phan-Thien (1985) successfully implemented the boundary element formulation to simulate extrusion flow experiments and Zheng and Phan-Thien (1992) used the method to study the unsteady motion of a sphere in a cylindrical tube containing a viscoelastic fluid. Also, Toose, Geurts and Kuerten (1995) recently performed simulations of two-dimensional viscoelastic drops in viscous flows using the boundary element method. To our knowledge there are no published simulations of the extensional dynamics of non-Newtonian liquid bridges (or filament stretching rheometers) where the temporal evolution of the interface shape, the applied force and the extensional viscosity are calculated.

The objective of this paper is thus to numerically explore the liquid filament stretching configuration in hope of discussing the validity of these techniques for calculating the extensional viscosity of complex fluids. The boundary element method is used to simulate the viscously dominated extension of axisymmetric, non-Newtonian liquid bridges. The non-Newtonian stresses in the fluid are modeled using the Oldroyd-B and the generalized upper-convected Maxwell constitutive equations. The simulations are compared with experimental results to investigate the effectiveness of these constitutive models, in a transient strong extensional flow.

We start by presenting the governing equations and a detailed discussion of different methods for computing the Trouton ratio in Section 2, followed, in Section 3, by a description of the numerical method. Results of the numerical simulations are presented in Section 4 and some conclusions are drawn in Section 5.

2
Mathematical model

The non-Newtonian fluids studied in filament stretching rheometers are typically very viscous liquids. The Reynolds number $\mathscr{R} = \rho U_0 L_0 / \eta_0$ characteristic of the experimental device used by Spiegelberg, Ables and McKinley (1996), with an initial end-plate separation of $L_0 = 2.2$ mm, an initial velocity $U_0 = 3.8$ mm/s and for a polystyrene-based polymer solution with material properties $\eta_0 = 47.7$ Pa · s and $\rho = 1026.0$ kg/m^3, is $\mathscr{R} = 1.8 \times 10^{-4}$. A Hencky strain of $\dot{\varepsilon}t = \ln(U/U_0) = 4.3$ can be achieved in this apparatus before the Reynolds number is of order one at which time inertial effects are expected to become significant. The theoretical treatment that follows is focused on the viscously dominated flow regime present in the experimental liquid bridge stretching device used by Spiegelberg, Ables and McKinley (1996), and we neglect fluid inertia.

A study of the dynamical evolution of a deforming liquid bridge involves solving for the shape of the free surface at every instant in time. This feature renders the problem nonlinear even for a Newtonian fluid at low
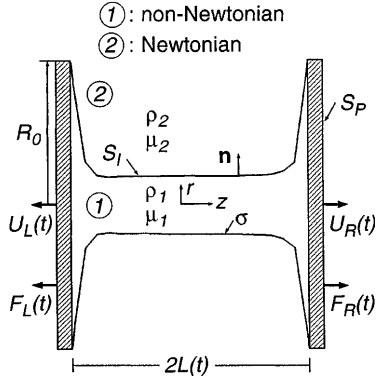
①: non-Newtonian
②: Newtonian

Fig. 2. Non-Newtonian liquid bridge undergoing steady stretching

Reynolds number and difficult to treat. The boundary element method is a well established method for simulating free surface flows involving Newtonian fluids in the viscous flow regime (Rallison and Acrivos (1978); Pozrikidis (1992)) and was successfully implemented to model the extensional deformation of Newtonian liquid bridges (Gaudet, McKinley and Stone (1996)). Bush (1984) reviewed the application of the boundary element method for the simulation of viscoelastic flow problems and presented a general derivation of the integral equation representation of the equations of motion. The principal stages of the development of the integral equations are summarized here and closely follow that presented by Bush (1984). We consider the elongation of a non-Newtonian liquid bridge as shown schematically in Fig. 2. Properties of the fluid filament are denoted with a subscript 1 and those of the surrounding fluid are denoted by 2. The external fluid is considered to be Newtonian and treated as unbounded so that the fluid has two internal boundaries, the fluid-fluid interface S_I and the end-plate surfaces S_P. We will restrict ourselves to axisymmetric bridge shapes so that the end plate fixtures are assumed to have an axisymmetric shape and, in particular, we focus attention on the case of infinitely thin, flat, circular disks shown in Fig. 2. The general analysis presented below allows for each end plate to move with an arbitrary prescribed velocity.

2.1
Integral representation of the momentum equation

The equations of motion for creeping flows of incompressible fluids inside or outside the liquid bridge are written as

$$\nabla \cdot \mathbf{T}_i = \mathbf{0} \quad \nabla \cdot \mathbf{u}_i = 0 \; , \tag{3}$$

where $i = 1, 2$, $\mathbf{u}$ is the velocity vector and the total stress tensor $\mathbf{T}$ is defined as

$$\mathbf{T} = \mathbf{T}^N + \mathbf{T}^{NN} \; . \tag{4}$$

The Newtonian stress tensor is defined so as to incorporate the modified pressure, $P - \rho \mathbf{g} \cdot \mathbf{x}$,

$$\mathbf{T}^N = -(P - \rho \mathbf{g} \cdot \mathbf{x})\mathbf{I} + \eta_s \dot{\gamma} \tag{5}$$

where η_s is the Newtonian fluid viscosity, ρ is the density, $\mathbf{g}$ denotes the gravitational acceleration, $\mathbf{x}$ denotes the

position vector, and $\dot{\gamma} = (\nabla \mathbf{u} + (\nabla \mathbf{u})^{\mathrm{T}})$ is the rate of strain tensor. The choice of constitutive relationship for the non-Newtonian extra stress tensor $\mathbf{T}^{NN} = \tau_{ij}\mathbf{e}_i\mathbf{e}_j$ will be discussed in Section 2.2.

The underlying assumption that is made when expressing the equations of motion for a non-Newtonian fluid in integral equation form is that the non-Newtonian effects in (3) can be treated as *pseudo-body* forces (Bush (1984)). Equation (3) is thus rewritten

$$\nabla \cdot \mathbf{T}_i^N = -\nabla \cdot \mathbf{T}_i^{NN} \quad \nabla \cdot \mathbf{u}_i = 0 \; , \tag{6}$$

and interpreted as Stokes equations subject to the body forces $\nabla \cdot \mathbf{T}_i^{NN}$. The outer fluid 2 is taken as a Newtonian fluid so $\mathbf{T}_2^{NN} = 0$ and we drop the subscript $i = 1$ indicating the non-Newtonian stress tensor for the inner fluid. The derivation now follows the standard approach used in expressing Stokes equations in integral form (Gaudet, McKinley and Stone (1996); Bush (1984); Rallison and Acrivos (1978); Pozrikidis (1992)). The integral equation representation of the solution is (assuming the velocity vanishes far away)

$$-\frac{1}{\eta_2} \int_{S_I+S_P} [\mathbf{n} \cdot \mathbf{T}_2 - \mathbf{n} \cdot \mathbf{T}_1] \cdot \mathbf{J}(\mathbf{x}|\mathbf{y}) \, \mathrm{d}S_y$$

$$+ (\lambda - 1) \int_{S_I+S_P} \mathbf{n} \cdot \mathbf{K}(\mathbf{x}|\mathbf{y}) \cdot \mathbf{u} \, \mathrm{d}S_y$$

$$+ \frac{1}{\eta_2} \int_{V_1} \mathbf{T}^{NN} : \nabla \mathbf{J}(\mathbf{x}|\mathbf{y}) \, \mathrm{d}V_y$$

$$= \begin{cases} \lambda \mathbf{u}_1(\mathbf{x}) & \mathbf{x} \in V_1 \\ \frac{1}{2}(1+\lambda)\mathbf{u}_1(\mathbf{x_s}) & \mathbf{x_s} \in S_I + S_P \\ \mathbf{u}_2(\mathbf{x}) & \mathbf{x} \in V_2 \end{cases} \; , \tag{7}$$

where η_s is the solvent viscosity for fluid 1, $\lambda = \eta_s/\eta_2$ is the viscosity ratio, $\mathbf{y}$ is the integration variable, and the tensors $\mathbf{J}$ and $\mathbf{K}$ are the Green's functions (Tanzosh, Manga and Stone (1992))

$$\mathbf{J}(\mathbf{x}|\mathbf{y}) = \frac{1}{8\pi}\left(\frac{\mathbf{I}}{r} + \frac{\mathbf{rr}}{r^3}\right),$$

$$\mathbf{K}(\mathbf{x}|\mathbf{y}) = -\frac{3}{4\pi}\frac{\mathbf{rrr}}{r^5} \text{ with } \mathbf{r} = \mathbf{x} - \mathbf{y}; r = |\mathbf{r}| \; . \tag{8}$$

The first term in equation (7) is divided into two integrals, one over S_I and the other over S_P. Use will also be made of the normal stress jump condition at a fluid-fluid interface,

$$\mathbf{n} \cdot \mathbf{T}_2 - \mathbf{n} \cdot \mathbf{T}_1 = \sigma(\nabla_s \cdot \mathbf{n})\mathbf{n} - \Delta \rho(\mathbf{g} \cdot \mathbf{x})\mathbf{n} \quad \mathbf{x_s} \in S_I \; , \tag{9}$$

where $\mathbf{n}$ is the unit normal directed into fluid 2, $\nabla_s = (\mathbf{I} - \mathbf{nn}) \cdot \nabla$ is the gradient operator along the interface, $\nabla_s \cdot \mathbf{n}$ is the mean interface curvature, the interfacial tension σ is assumed constant, and $\Delta\rho = \rho_1 - \rho_2$. The stress jump across the rigid end plates is denoted $\mathbf{f} = \mathbf{n} \cdot \mathbf{T}_2 - \mathbf{n} \cdot \mathbf{T}_1$ on S_P.

The integral equation (7) may now be nondimensionalized by choosing U_{R0}, R_0 and $\eta_s U_{R0}/R_0$, respectively, as the characteristic velocity, length and stress. Here the initial velocity of the right-hand end plate is denoted by U_{R0}. Equation (7) is expressed in dimensionless form

(using the same variables as above for their dimensionless counterparts) as

$$-\frac{1}{\mathscr{C}}\int_{S_I}[\mathbf{n}(\nabla_s\cdot\mathbf{n})-\mathscr{B}(\mathbf{e}_g\cdot\mathbf{y})\mathbf{n}]\cdot\mathbf{J}(\mathbf{x}|\mathbf{y})\,dS_y$$

$$+\left(1-\frac{1}{\lambda}\right)\int_{S_I+S_P}\mathbf{n}\cdot\mathbf{K}(\mathbf{x}|\mathbf{y})\cdot\mathbf{u}\,dS_y$$

$$+\int_{V_1}\mathbf{T}^{NN}:\nabla\mathbf{J}(\mathbf{x}|\mathbf{y})\,dV_y-\int_{S_P}\mathbf{f}\cdot\mathbf{J}(\mathbf{x}|\mathbf{y})\,dS_y$$

$$=\begin{cases}\mathbf{u}_1(\mathbf{x}) & \mathbf{x}\in V_1\\ \frac{1}{2}\left(1+\frac{1}{\lambda}\right)\mathbf{u}_1(\mathbf{x}_s) & \mathbf{x}_s\in S_I+S_P\ ,\\ \frac{1}{\lambda}\mathbf{u}_2(\mathbf{x}) & \mathbf{x}\in V_2\end{cases}\qquad(10)$$

where $\mathbf{e}_g$ is a unit vector in the direction of gravity. As a result of expressing (7) in a dimensionless form, two parameters, the capillary number $\mathscr{C}$ and the Bond number $\mathscr{B}$,

$$\mathscr{C}=\frac{\eta_s U_{R0}}{\sigma}\qquad\mathscr{B}=\frac{\Delta\rho g R_0^2}{\sigma}\qquad(11)$$

which represent, respectively, the relative magnitudes of viscous and gravitational body forces to interfacial tension forces, appear as two relevant dimensionless groupings in the problem. The viscosity ratio λ and the Deborah number $\mathscr{D}$, which will be introduced in Section 2.2, are the other important dimensional groups. In the present work we are primarily interested in the effects of viscoelasticity on the evolution of the column rather than the perturbations arising from an outer fluid viscosity. Hence, the viscosity ratio is held constant at $\lambda=2.0\times10^6$, corresponding to the case of the inner viscous experimental test fluid and air as the outer fluid. The effects of varying λ on the evolution of a Newtonian fluid column have been investigated elsewhere by Gaudet, McKinley and Stone (1996), and for $\lambda>100$ the outer fluid has negligible effect on the column dynamics.

Boundary conditions are specified on the end plates where the velocities are $\mathbf{u}(\mathbf{x}_s\in S_P)=\mathbf{U}_L(t)$ on the left end plate and $\mathbf{u}(\mathbf{x}_s\in S_P)=\mathbf{U}_R(t)$ on the right end plate. Specification of an initial surface configuration completes the problem statement. Assuming the stress tensor $\mathbf{T}^{NN}$ at any time is known, the solution of integral equation (10), defined over the bounding surfaces S_P and S_I, yields the stress jump distribution on the end plates $\mathbf{f}(\mathbf{x}_s\in S_P)$ and the interfacial velocities $\mathbf{u}(\mathbf{x}_s\in S_I)$ from which the shape of the liquid bridge can be determined as a function of time.

2.2
Constitutive equation
In this work we use the generalized upper-convected Maxwell model (Bird, Armstrong and Hassager (1987)) together with an additional solvent contribution to compute the evolution of the viscoelastic stresses in the fluid. In dimensional terms the stresses are written in terms of a Newtonian contribution $\mathbf{T}^N$ and a polymeric contribution $\mathbf{T}^{NN}$ as:

$$\mathbf{T}^N=\eta_s\dot{\gamma}$$

$$\mathbf{T}^{NN}=\sum_i^{N_{\text{modes}}}\mathbf{T}_i^{NN}\qquad(12)$$

$$\mathbf{T}_i^{NN}+\lambda_i\mathbf{T}_{i(1)}^{NN}=\eta_{ip}\dot{\gamma}\ ,$$

where λ_i are the spectrum of elastic time constants or relaxation times of the polymer, η_{ip} are the corresponding polymeric viscosities for each mode and the subscript (1) denotes an upper-convected derivative (Bird, Armstrong and Hassager (1987))

$$\mathbf{T}_{(1)}^{NN}=\frac{\partial\mathbf{T}^{NN}}{\partial t}+\mathbf{u}\cdot\nabla\mathbf{T}^{NN}-(\nabla\mathbf{u})^{\mathrm{T}}\cdot\mathbf{T}^{NN}-\mathbf{T}^{NN}\cdot\nabla\mathbf{u}\ .$$
$$(13)$$

When a single mode is used in (12), the resulting constitutive equation is the well known *Oldroyd-B* or *upper-convected Jeffreys* model

$$\mathbf{T}^N=\eta_s\dot{\gamma}\quad\mathbf{T}^{NN}+\lambda_1\mathbf{T}_{(1)}^{NN}=\eta_p\dot{\gamma}\ ,\qquad(14)$$

where λ_1 is the single elastic time constant and η_p is the polymeric contribution to the total viscosity of the inner fluid. The dimensionless form (again using the same variables) of the constitutive equation is

$$\mathbf{T}^N=\dot{\gamma}\quad\mathbf{T}_i^{NN}+2\Lambda_0\mathscr{D}_i\mathbf{T}_{i(1)}^{NN}=\beta_{ip}\dot{\gamma}\ ,\qquad(15)$$

and can be obtained by again choosing the initial velocity of the right-hand end plate U_{R0} as the characteristic velocity and R_0, $\eta_s U_{R0}/R_0$ and R_0/U_{R0}, respectively, as the characteristic length, stress and time scales. The initial aspect ratio of the liquid bridge is denoted by $\Lambda_0=L_0/R_0$ and $\beta_{ip}=\eta_{ip}/\eta_s$. The dimensionless number that characterizes the relative importance of the elastic stresses in equation (15) to viscous stresses is the Deborah number,

$$\mathscr{D}_i=\lambda_i\dot{E}\ ,\qquad(16)$$

where $\dot{E}=U_{R0}/2L_0$ is the characteristic dimensional axial extension rate conventionally chosen. The aspect ratio also arises in (15) as a result of the choice of the length scale $2L_0$ in the definition of $\dot{E}$. The natural time scale arising from the chosen scaling for velocity and length is the convective scale R_0/U_{R0}. However, for consistency with existing experimental work (Tirtaatmadja and Sridhar (1993); Spiegelberg, Ables and McKinley (1996)) we present results in this paper using the axial Hencky strain

$$\varepsilon=\ln\left(\frac{L(t)+L_0}{2L_0}\right)=\dot{E}t\ .$$

The Oldroyd-B equation is a three parameter model that predicts a constant shear viscosity $\eta_0=\eta_p+\eta_s$ and first normal stress coefficient $\Psi_{10}=2\eta_p\lambda_1$ in steady shear flow and a strain-rate-dependent extensional viscosity in transient uniaxial elongation (Bird, Armstrong and Hassager (1987)). Another feature of the upper-convected Jeffreys model is that for a Deborah number $\mathscr{D}>0.5$ the axial stresses in a homogeneous uniaxial elongational flow grow unbounded in time and a steady state value of the extensional viscosity cannot be achieved (Bird, Armstrong and Hassager (1987)). Extensional rheometers are designed to

be dominated by extensional kinematics and to be free of shearing motions and the Oldroyd-B model has been shown to be a reasonable choice as a constitutive equation for these flows (Keiller (1992a, 1992b)). Keiller (1992a, 1992b) used the Oldroyd-B model to qualitatively and quantitatively simulate some of the many extensional viscosity measurements performed on international test standard fluid denoted 'M1' (James and Walters (1993)). The Oldroyd-B model does have the limitation that stresses may grow unbounded at large strains but steady state values of the extensional viscosity are difficult to achieve in the experiments (Spiegelberg, Ables and McKinley (1996)), and it does capture the transient exponential stress growth in regions of a complex flow where uniaxial extension kinematics are dominant.

We use a cylindrical polar coordinate system and for an axisymmetric elongating column, only four of the components of the non-Newtonian extra stress tensor (for mode i) $\mathbf{T}_i^{NN} = \tau_{i\alpha\beta}\mathbf{e}_\alpha\mathbf{e}_\beta$, $\tau_{irr}, \tau_{izz}, \tau_{irz}$ and $\tau_{i\theta\theta}$, are expected to be independent and non-zero ($\tau_{irz} = \tau_{izr}$, $\tau_{ir\theta} = \tau_{i\theta r} = 0$, $\tau_{iz\theta} = \tau_{i\theta z} = 0$). Four coupled partial differential equations thus result from (15) and are written as

$$\tau_{irr} + 2\Lambda_0\mathscr{D}_i\left\{\frac{D\tau_{irr}}{Dt} - 2\tau_{irr}\frac{\partial u_r}{\partial r} - 2\tau_{irz}\frac{\partial u_r}{\partial z}\right\} = 2\beta_{ip}\frac{\partial u_r}{\partial r}$$

$$\tau_{izz} + 2\Lambda_0\mathscr{D}_i\left\{\frac{D\tau_{izz}}{Dt} - 2\tau_{izz}\frac{\partial u_z}{\partial z} - 2\tau_{irz}\frac{\partial u_z}{\partial r}\right\} = 2\beta_{ip}\frac{\partial u_z}{\partial z}$$

$$\tau_{irz} + 2\Lambda_0\mathscr{D}_i\left\{\frac{D\tau_{irz}}{Dt} - \tau_{irz}\frac{\partial u_r}{\partial r} - \tau_{izz}\frac{\partial u_r}{\partial z}\right. \tag{17}$$

$$\left. -\tau_{irr}\frac{\partial u_z}{\partial r} - \tau_{irz}\frac{\partial u_z}{\partial z}\right\} = \beta_{ip}\left(\frac{\partial u_z}{\partial r} + \frac{\partial u_r}{\partial z}\right)$$

$$\tau_{i\theta\theta} + 2\Lambda_0\mathscr{D}_i\left\{\frac{D\tau_{i\theta\theta}}{Dt} - 2\tau_{i\theta\theta}\frac{u_r}{r}\right\} = 2\beta_{ip}\frac{u_r}{r} \quad,$$

where D/Dt is the usual material derivative.

In order to integrate this system of equations in time, initial values for the four stress components $\tau_{irr}^{(0)}, \tau_{izz}^{(0)}, \tau_{irz}^{(0)}$ and $\tau_{i\theta\theta}^{(0)}$ are required as well as knowledge of the velocity vector $\mathbf{u}$ everywhere inside the liquid bridge volume V_1. Simultaneous solutions of equations (10) and (17) will be discussed in Section 3. We now turn to a discussion of the calculation of the extensional viscosity and the Trouton ratio.

2.3
Trouton ratio
In Section 1 a definition for the extensional viscosity was introduced for an ideal shear-free flow (see equation (2)). The transient Trouton ratio (Trouton (1906)), which compares the relative importance of the extensional viscosity in a homogeneous transient elongational flow with the shear viscosity, is expressed in terms of the tensile stress difference at extension rate $\dot{E}$

$$Tr^+ = \frac{T_{zz} - T_{rr}}{\eta_0\dot{E}} \quad. \tag{18}$$

In terms of the dimensionless Newtonian and polymeric contributions to the total tensile stress, equation (18) becomes

$$Tr^+ = 2\Lambda_0\frac{\eta_s}{\eta_0}[(\tau_{zz} - \tau_{rr}) + (\dot{\gamma}_{zz} - \dot{\gamma}_{rr})] \quad. \tag{19}$$

If the imposed axial extension rate $\dot{E}$ in an extensional rheometer is constant in time and the kinematics of the flow given by equation (1) are realized then an initially cylindrical volume of fluid will deform as a cylinder and each component of stress is spatially and temporally homogeneous. However, the flow field generated by the liquid bridge stretching device is not free of shearing motions as a result of the rigid end plates and the extensional deformation rate $\dot{\gamma}_{zz}$ varies throughout the flow domain. The question of how to best calculate the extensional viscosity and the Trouton ratio for an actual liquid bridge stretching experiment thus arises.

The quantity most easily measured in a laboratory experiment is the force required to maintain the left end plate stationary. Referring to Fig. 3a, a force balance on the left end plate yields the dimensionless equation

$$\mathscr{F}_L = \frac{F_L}{\eta_s U_{R0}R_0} = -\mathscr{F}_{vis} - \frac{2\pi}{\mathscr{C}\left(1 + \left(\frac{\partial x}{\partial z}\right)^2_{z=-\Lambda_0}\right)^{1/2}} \quad,$$

$$\tag{20}$$

where the first term $\mathscr{F}_{vis} = \int_{S_P}\mathbf{n}\cdot[\mathbf{n}\cdot\mathbf{T}_2 - \mathbf{n}\cdot\mathbf{T}_1]\,dS$ is the total viscoelastic force contribution obtained by integrating the normal stress jump on the end-plate surface S_P and the second term represents the integrated contribution from interfacial tension forces on the left end plate denoted by $\mathscr{F}_\sigma$ on Figures 3a and 3b. The dimensionless profile of the free surface is denoted by $x \equiv R(z)/R_0$. The stress jump is one of the unknowns of integral equation (10) while the slope of the interface $\partial x/\partial z$ is obtained at the left end plate as the interface evolves in time. We note that all dimensionless forces and stresses in this paper are scaled with the solvent viscosity η_s, rather than the total viscosity.

A *true* Trouton ratio can be defined as

$$Tr_{true} = \frac{2\Lambda_0\eta_s\mathscr{F}_{vis}}{\eta_0\pi} \quad, \tag{21}$$
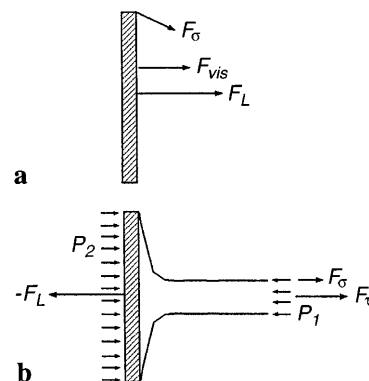

a

b

Fig. 3. a Force balance on the left end plate b Force balance on a control volume containing half of the liquid bridge; $\mathscr{F}_\tau = \dot{\gamma}_{zz1} + \tau_{zz1}$, and $\mathscr{F}_\sigma$ is the integrated contribution from interfacial tension forces at the perimeter of the left end plate

where $A_P = \pi$ is the dimensionless left end-plate area. However, the Trouton ratio expressed in (21) cannot be used as it is and has to be modified to correct for inter-facial tension effects which are present in the pressure difference term contributing to the total traction on the left-hand end plate.

For a deforming cylinder in a uniaxial extensional flow field, and in a case where there is no interfacial tension ($\mathscr{C} \to \infty$) and the viscosity ratio is large ($\lambda \gg 1$), $P_1 - P_2 = \dot{\gamma}_{rr1} + \tau_{rr1}$ (given by (9)) and $\mathrm{Tr}_{\mathrm{true}}$ reduces to (19). However, for finite interfacial tension on the fluid-fluid interface and a liquid bridge geometry with solid end plates, the expression (21) contains capillary effects in the pressure difference term contributing to $\mathscr{F}_{\mathrm{vis}}$. If the assumption is made that the pressure inside the liquid column, P_1, varies very little in the radial direction, then the stress jump on the interface (9) can be used to express the dimensionless pressure difference as

$$P_1 - P_2 = \dot{\gamma}_{rr1} + \tau_{rr1} + \frac{\kappa_L}{\mathscr{C}} \quad , \tag{22}$$

where κ_L is the dimensionless interfacial curvature at the left end plate. Using (22) to remove the capillary pressure contribution to the total end-plate force leads to an alternative definition for the Trouton ratio (Gaudet (1996)) but will not be presented here because shearing effects would still be present in $\mathscr{F}_{\mathrm{vis}}$.

We will see in Section 4 that in the middle of the fluid column, after a certain strain, a nearly shear-free region develops. A force balance, based on the control volume shown in Fig. 3b, can thus be written so as to exploit this extensionally dominated region however this expression requires explicit information about the evolution of the middle of the liquid bridge. The Trouton ratio, based on this information can be written

$$\mathrm{Tr}_{\mathrm{mid}} = -\frac{2\Lambda_0 \eta_s \left(\mathscr{F}_L - \frac{\pi X_{\mathrm{mid}}}{\mathscr{C}} \right)}{\pi \eta_0 X_{\mathrm{mid}}^2} \quad , \tag{23}$$

where $X_{\mathrm{mid}}(t)$ is the dimensionless mid-point radius. The advantages of expression (23) are that the curvature in the middle of a strain-hardened and fore-aft symmetric filament is given by the inverse of the minimum filament radius and the assumption of no radial dependence of the pressure is a much better one in this region. The final remaining disadvantage of (23) is that the extension rate used to calculate the Trouton ratio is the imposed axial extension rate $\dot{E}$ which is not the actual strain rate realized in the middle of the fluid column. An improved version of (23) is thus obtained by replacing the imposed strain rate $\dot{E}$ by the effective strain rate in the middle of the liquid sample,

$$\mathrm{Tr}_{\mathrm{eff}} = -\frac{2\Lambda_0 \eta_s \dot{E} \left(\mathscr{F}_L - \frac{\pi X_{\mathrm{mid}}}{\mathscr{C}} \right)}{\pi \eta_0 \dot{\varepsilon}_{\mathrm{eff}} X_{\mathrm{mid}}^2} \quad , \tag{24}$$

where

$$\dot{\varepsilon}_{\mathrm{eff}} = \frac{-2 u_r(X_{\mathrm{mid}})}{X_{\mathrm{mid}}} \equiv -\frac{2}{X_{\mathrm{mid}}} \frac{\mathrm{d}X_{\mathrm{mid}}}{\mathrm{d}t}$$

is the dimensionless effective radial strain rate in the middle of the fluid column.

A final point-wise Trouton ratio can be defined which also uses the actual strain rate at the middle of the liquid bridge where shearing effects are minimal,

$$\mathrm{Tr}_{\mathrm{point}} = \frac{\eta_s (\dot{\gamma}_{zz} + \tau_{zz} - (\dot{\gamma}_{rr} + \tau_{rr}))|_{x=0, z=\mathrm{mid}}}{\eta_0 \dot{\varepsilon}_{\mathrm{eff}}} \quad . \tag{25}$$

Expression (25) generates a point-wise Trouton ratio at the point $x = 0, z = L(t)$; but is difficult to use experimentally since point-wise dynamical data for the evolving polymeric stresses is difficult to obtain.

The validity of expressions (23–25) for Trouton ratio will be compared and discussed in Section 4.

3
Numerical implementation

3.1
Discretization of the bounding surfaces

The governing integral equation (10) contains both surface and volume integrals. Because of the axisymmetric nature of the problem, the azimuthal integration of all the integrands in (10) can be performed analytically reducing all surface integrals to line integrals and the volume integrals to surface integrals. At a given time, the fluid-fluid interface need only be described by a one-dimensional function $X(z) = R(z)/R_0$ and subdivided into N_I line elements. On each of the end plates, N_P line elements are defined. A constant element boundary integral formulation is utilized whereby the unknown velocities $\mathbf{u}(\mathbf{x} \in S_I)$ and stress jump $\mathbf{f}(\mathbf{x} \in S_P)$ are assumed constant on each element. The nodal points where unknowns are evaluated are defined at the middle of the surface elements. The interface shape $X = X(z)$ is approximated by a cubic spline interpolant with which second derivatives are evaluated in order to obtain the surface curvature $\kappa(z)$.

The discretization of the two-dimensional surface of revolution of the liquid bridge, which we will henceforth call the flow domain, is independent of the discretization of the interface $X(z)$ and is discussed in the following paragraph.

3.2
Mapping

At every instant in time, the flow domain is mapped onto a rectangular domain whose length increases with time. The discretization of the mapped domain is shown in Fig. 4. We define N_X surface elements in the radial direction and N_Z in the axial direction. Velocities and stresses are defined at the center of the surface elements and are assumed constant on these elements.

At any instant in time t, the flow domain (x, z) is mapped onto the rectangular domain (S, T) according to the following linear transformation:

$$S(x, z) = \frac{x}{X(z)} \quad T(z) = z \quad , \tag{26}$$

where $0 \leq S \leq 1$ at all points along column, and $-\Lambda_0 \leq T \leq 2\Lambda - \Lambda_0$ and where we have neglected to indicate the time dependence of the transformation. The mapping transformation is simple and the two-dimensional integrations are all performed on the rectangular
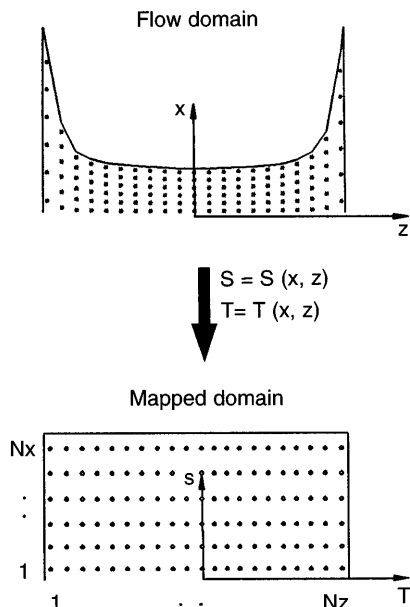
Fig. 4. Discretization of the flow and mapped domains

mapped domain where the IMSL two-dimensional spline routines for rectangular grids can be used. A simple change of variables for double integrals (Kreyszig (1993)) is used to perform the two-dimensional integration of the non-Newtonian term according to

$$\int_z \int_x G(x,z)\,\mathrm{d}x\,\mathrm{d}z = \int_T \int_S G(x(S,T),\,z(S,T))|J|\,\mathrm{d}S\,\mathrm{d}T \; ,$$

(27)

where $G(x,z)$ represents the non-Newtonian integrand in (10) after the azimuthal integration and J is the Jacobian of the transformation, which using (26) becomes

$$J \equiv \begin{vmatrix} \frac{\partial x}{\partial S} & \frac{\partial x}{\partial T} \\ \frac{\partial z}{\partial S} & \frac{\partial z}{\partial T} \end{vmatrix} = X(z) \; .$$

(28)

When equation (10) is used to determine the velocities inside V_1, the integrand $G(x(S,T), z(S,T))$ becomes singular at each of the points where the velocities are sought. The *degenerate quadrilaterals* method (Lucas (1995)) is used to eliminate the singularities at these points. Two-dimensional splines are used to represent the velocity field in the mapped domain and to calculate derivatives of velocity with respect to the transformation variables S and T. The derivatives of velocity in the physical domain are required in (17) and are obtained using the chain rules,

$$\left(\frac{\partial u_r}{\partial z}\right)_x = -\frac{x}{X(z)^2}\frac{\mathrm{d}X}{\mathrm{d}z}\left(\frac{\partial u_r}{\partial S}\right)_T + \left(\frac{\partial u_r}{\partial T}\right)_S$$

$$\left(\frac{\partial u_r}{\partial x}\right)_z = \frac{1}{X(z)}\left(\frac{\partial u_r}{\partial S}\right)_T$$

$$\left(\frac{\partial u_z}{\partial z}\right)_x = -\frac{x}{X(z)^2}\frac{\mathrm{d}X}{\mathrm{d}z}\left(\frac{\partial u_z}{\partial S}\right)_T + \left(\frac{\partial u_z}{\partial T}\right)_S$$

$$\left(\frac{\partial u_z}{\partial x}\right)_z = \frac{1}{X(z)}\left(\frac{\partial u_z}{\partial S}\right)_T \; .$$

(29)

3.3
Initial and boundary conditions
Two sets of initial conditions are required for this problem: 1) values for the four components of the non-Newtonian stress and 2) an initial interface shape specified by $R(z, t = 0)$. In this paper, results will be presented for the initial conditions: $\tau_{irr}^{(0)} = 0, \tau_{izz}^{(0)} = 0, \tau_{irz}^{(0)} = 0, \tau_{i\theta\theta}^{(0)} = 0$ and $X(z, t = 0) = 1$. This corresponds to the typical experimental configuration in which a liquid sample is placed between the plates and allowed to equilibrate for a period corresponding to several relaxation times. We show below that in a strong stretching motion this initial data can influence the column dynamics and care must be taken to ensure a preshear history does not contaminate measurement of the transient evolution in the viscoelastic stresses.

At a given time step, knowledge of the shape of the interface and its curvature everywhere are required, as are the velocities of the two end plates. As mentioned above, a cubic spline interpolant provides all the information required on the interface including the curvature which enters in the first term of equation (10). The dimensional end-plate velocity boundary conditions imposed in all of our simulations (except a validation case described in Section 4 and for the velocity compensation study of Section 4.2.3) are $u_z(z = L(t)) = U_{R0} \exp(\dot{E}t)$ and $u_r = 0$. The simulations start with a fully relaxed cylinder of a non-Newtonian fluid having no elastic stress history and the cylinder then undergoes quasi-steady extensional motion driven by the right-hand end plate that is translating at a velocity which increases exponentially with time.

3.4
Algorithm
We will now present the details of the numerical procedure. We note that equations (17) are rewritten in the form $\mathrm{D}\tau_{i\alpha\beta}/\mathrm{D}t = g_{i\alpha\beta}$. The time-dependent boundary element formulation for the deformation of a viscoelastic fluid with a deformable free surface are solved in the following sequence of steps:

i. Impose the initial conditions (interface shape, $\mathbf{T}^{NN}$), the time step Δt and boundary conditions.
ii. Write the discretized version of equation (10) successively for N_I points on the interface and the $2N_P$ points on the two end plates. A $2(N_I + 2N_P) \times 2(N_I + 2N_P)$ system of linear equations is thus obtained and solved using standard linear system solvers. The velocities on the interface and the stress jump on the end plates are thus obtained.
iii. With the velocities and stress jump values obtained in step (ii), calculate velocities at each node point in the internal domain using equation (10).
iv. Using the velocities calculated in step (iii), integrate the system of equations (17) forward in time using the explicit fourth-order Adams-Bashforth method (Burden and Faires (1985)). For example at node point jk,

$$\left(\tau_{irr}^{(t+\Delta t)}\right)_{jk} = \left(\tau_{irr}^{(t)} + \frac{\Delta t}{24}[55g_{irr}(t) - 59g_{irr}(t-\Delta t) \right.$$
$$\left. + 37g_{irr}(t-2\Delta t) - 9g_{irr}(t-3\Delta t)]\right)_{jk} \; .$$

Notes: As we have previously mentioned, a Lagrangian integration is used for the stresses. An explicit Euler time step (still a Lagrangian integration but using Euler's method) is used to generate the first values of $g_{i\alpha\beta}(t-\Delta t)$, $g_{i\alpha\beta}(t-2\Delta t)$ and $g_{i\alpha\beta}(t-3\Delta t)$. Here time has also been nondimensionalized with the convective time scale R_0/U_{R0}.

v. Move (in a Lagrangian sense) the interface and the internal *Lagrangian* nodes using the explicit fourth-order Adams-Bashforth method:

$$
\begin{aligned}
x_i^{(t+\Delta t)} &= x_i^{(t)} + \frac{\Delta t}{24}[55u_r(t) - 59u_r(t-\Delta t) \\
&\quad + 37u_r(t-2\Delta t) - 9u_r(t-3\Delta t)] \\
z_i^{(t+\Delta t)} &= z_i^{(t)} + \frac{\Delta t}{24}[55u_z(t) - 59u_z(t-\Delta t) \\
&\quad + 37u_z(t-2\Delta t) - 9u_z(t-3\Delta t)] \ .
\end{aligned}
\tag{30}
$$

vi. Compute values of the Trouton ratio using equations (23)–(25).

vii. Using the stresses obtained in step (iv) repeat steps (ii) to (v).

We will now present results of the numerical implementation of the above algorithm to equations (10) and (17).

4
Numerical results
In this section we present results of our numerical simulations of the stretching of non-Newtonian liquid bridges, an example of which has been shown above in Fig. 2. In the results reported here, gravitational body forces are neglected, i.e., $\mathscr{B} = 0$; it is nevertheless straightforward to solve (10) and (17) for axisymmetric geometries with $\mathscr{B} \neq 0$. Numerical convergence checks have been performed to ensure convergence with time step as well as with spatial discretization.

4.1
Validation case: homogeneous extensional flow
The transient evolution of the non-Newtonian stresses for an ideal extensional flow (1) can be obtained analytically (Bird, Armstrong and Hassager (1987)), by integrating the Oldroyd-B equation, and expressed in dimensionless form

$$
\begin{aligned}
\tau_{rr} &= \frac{1+\beta_p+\mathscr{D}}{2\Lambda_0(1+\mathscr{D})} - \frac{1}{2\Lambda_0}\left[\frac{1+\beta_p+\mathscr{D}}{1+\mathscr{D}} - 1 - 2\Lambda_0\tau_{rr}^{(0)}\right] \\
&\quad \times \exp\left\{-\frac{t}{2\Lambda_0\mathscr{D}}(1+\mathscr{D})\right\} \\
\tau_{zz} &= -\frac{(1+\beta_p)}{\Lambda_0(1-2\mathscr{D})} + \frac{2\mathscr{D}}{\Lambda_0(1-2\mathscr{D})} \\
&\quad + \frac{1}{\Lambda_0}\left[\frac{1+\beta_p}{1-2\mathscr{D}} - \frac{2\mathscr{D}}{1-2\mathscr{D}} - 1 + \Lambda_0\tau_{zz}^{(0)}\right] \\
&\quad \times \exp\left\{-\frac{t}{2\Lambda_0\mathscr{D}}(1-2\mathscr{D})\right\} \ ,
\end{aligned}
\tag{31}
$$

where $\tau_{rr}^{(0)} = \tau_{rr}(0)$ and $\tau_{zz}^{(0)} = \tau_{zz}(0)$ are the initial radial and axial stresses, respectively. For the numerical results that follow, $\tau_{rr}^{(0)} = \tau_{zz}^{(0)} = 0$. This one-dimensional flow can

also be numerically simulated with the two-dimensional algorithm presented in Section 2 and 3 by relaxing the no-slip boundary condition on S_P allowing the fluid particles adjacent to the end plates to move radially inwards as well as axially. We simply impose the dimensionless form of (1) as the velocity boundary conditions on both end plates:

$$
\mathbf{u}(x, z = -\Lambda_0) = -\frac{1}{4}\frac{x}{\Lambda_0}\mathbf{e}_x
$$

$$
\mathbf{u}(x, z = 2\Lambda(t) - \Lambda_0) = -\frac{1}{4}\frac{x}{\Lambda_0}\mathbf{e}_x + \exp(\dot{E}t)\mathbf{e}_z \ ,
$$

where $2\Lambda(t)$ is the instantaneous dimensionless length of the liquid bridge, x is the dimensionless radial coordinate on the end plates and $\mathbf{e}_x$ and $\mathbf{e}_z$ are unit vectors in the radial and axial directions, respectively. In a laboratory this boundary motion could be achieved by having end plates that are made of a compressible sponge-like or stretched elastomeric material, for example. Berg, Kröger and Rath (1994) performed this experiment using an elastic diaphragm.

In Fig. 5 we show the results of our numerical simulations for a liquid bridge whose end plates are deforming
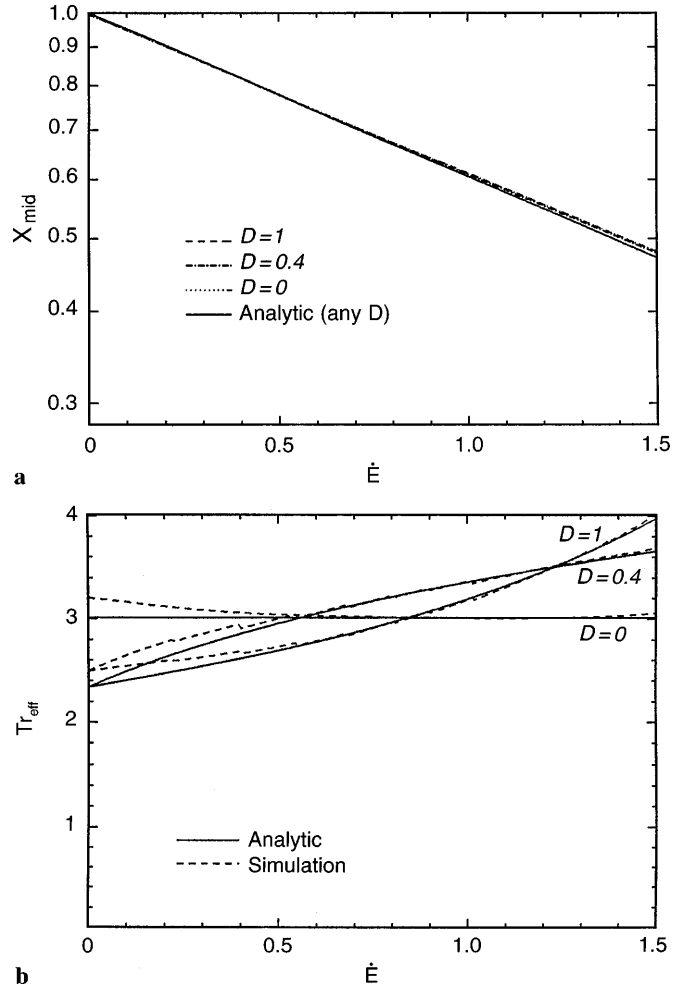
Fig. 5. Evolution of **a** the mid-point radius and **b** the effective Trouton ratio; $\mathscr{C} = 1.0 \times 10^9$, $\lambda = 2.0 \times 10^6$, $\Lambda_0 = 1$, $\beta_p = 0.28$ and $\mathscr{B} = 0$. The curves for $\mathscr{D} = 1$, $\mathscr{D} = 0.4$ and $\mathscr{D} = 0$ superpose in **a**

according to an ideal extensional flow. For these results the Oldroyd-B model was used. In Fig. 5a we show the evolution of the liquid bridge mid-point radius for various values of the Deborah number $\mathscr{D}$. The dashed line in this figure represents the radial evolution at any Deborah number $\mathscr{D}$. The initial interface configuration for all the computations in this paper is that of a cylinder, characterized by its initial aspect ratio Λ_0. The predicted radial evolution for an ideal extensional flow follows a straight line on a semi-logarithmic plot with slope $-\dot{E}/2$. The results of the numerical simulations nearly superpose with the analytical results for all the values of $\mathscr{D}$ computed which indicates the simulated flow kinematics are the same as an ideal extensional flow.

The transient effective Trouton ratio (expression (24)) result for the same values of $\mathscr{D}$ is shown in Fig. 5b. Agreement with the analytic Trouton ratio is almost perfect for strains larger than $\dot{E}t = 0.5$. Our numerical results show that the stress-jump (or force) distribution on the end plates is not uniform for small values of the initial aspect ratio Λ_0 and that this variation from the center of the end plate to the perimeter diminishes as the liquid bridge is extended. The other expressions for the Trouton ratio introduced in Section 2.3 are not presented, but as expected, all reduce to the same value for $\mathscr{C} = \infty$ and a very large viscosity ratio. We also mention that the stress growth for the case $\mathscr{D} = 0.4$ at early strains is faster than for $\mathscr{D} = 1$ due to the linear viscoelastic response of the fluid and the non-dimensional scaling chosen for time but eventually approaches a plateau whereas the Trouton ratio in the other case grows unbounded.

The numerical results presented in this section, apart from the discrepancies at very small strains, are in excellent agreement with the analytic expressions (31) and (1). In the process of generating results for this validation case, every aspect of the algorithm presented in Section 3.4 was tested and appeared to perform well so we now turn to the simulation of filament stretching devices.

4.2
Numerical simulations of the filament stretching device
In this section we present results of our numerical simulations of the filament stretching device used by Sridhar, Tirtaatmadja, Nguyen and Gupta (1991) and Spiegelberg, Ables and McKinley (1996). In addition to exploring the general trends of the predicted response using the Oldroyd-B model, the numerical results will also be compared to a stretching experiment conducted by Spiegelberg, Ables and McKinley (1996). In these experiments, the end-plate radius was $R_0 = 3.5\,\mathrm{mm}$ for both disks and the viscoelastic test solution consisted of a high-molecular weight polystyrene solute (polymer) in a low-molecular weight polystyrene solvent. The parameters for the four-mode model obtained from regression to linear viscoelastic data are: $\lambda_1 = 2.414\,\mathrm{s}$, $\lambda_2 = 0.91\,\mathrm{s}$, $\lambda_3 = 0.096\,\mathrm{s}$, $\lambda_4 = 6.4 \times 10^{-3}\,\mathrm{s}$, $\eta_{1p} = 2.2\,\mathrm{Pa} \cdot \mathrm{s}$, $\eta_{2p} = 1.02\,\mathrm{Pa} \cdot \mathrm{s}$, $\eta_{3p} = 0.77\,\mathrm{Pa} \cdot \mathrm{s}$ and $\eta_{4p} = 1.52\,\mathrm{Pa} \cdot \mathrm{s}$. The solvent viscosity of the polystyrene solvent is $\eta_s = 37.2\,\mathrm{Pa} \cdot \mathrm{s}$. These parameters were obtained from viscometric shear measurements on the polystyrene solution and the resulting Deborah numbers, given an imposed axial extension rate of $\dot{E} = 1.72\,\mathrm{s}^{-1}$, are:

$\mathscr{D}_1 = 4.15$, $\mathscr{D}_2 = 1.56$, $\mathscr{D}_3 = 0.17$ and $\mathscr{D}_4 = 1.1 \times 10^{-2}$. Hence the first and second modes are expected to exhibit significant elastic stress growth, whereas the shorter relaxation modes ($\mathscr{D}_i < 1/2$) will contribute only to the linear viscoelastic response of the system.

4.2.1
Oldroyd-B model
We first present, in Fig. 6, a comparison of the evolution of the liquid filament interface for two cases, a Newtonian liquid (Fig. 6a) and a non-Newtonian liquid described by a single-mode Oldroyd-B fluid model (Fig. 6b). The stretch rate in the experiment was $\dot{E} = 1.72\,\mathrm{s}^{-1}$ and will be used for all the numerical computations in this paper. The Deborah number $\mathscr{D}$, for the single mode result in Fig. 6b, is $\mathscr{D} = 6.0$ and we show this figure in order to highlight the difference fluid elasticity makes in the kinematics of an extending liquid bridge. In fact, strain hardening in the non-Newtonian filament is responsible for suppressing the accelerated pinching that occurs in the Newtonian filament and leads to the formation of an almost cylindrical region in the middle of the filament (whose length increases with time). In this region the flow is nearly shear-free, which is a necessary feature for an extensional rheometer. Alignment and extension of the macromolecules in the direction of stretching increases the tensile force in the fluid thread and, inhibits further elongation in the narrowest section of the filament. Radial displacement of fluid elements thus becomes easier away from the middle of the fluid filament in regions where the tensile stresses are lower and formation of an increasingly uniform cylindrical region results. These kinematic observations have been well documented in the experimental literature (Sridhar, Tirtaatmadja, Nguyen and Gupta (1991); Tirtaatmadja and
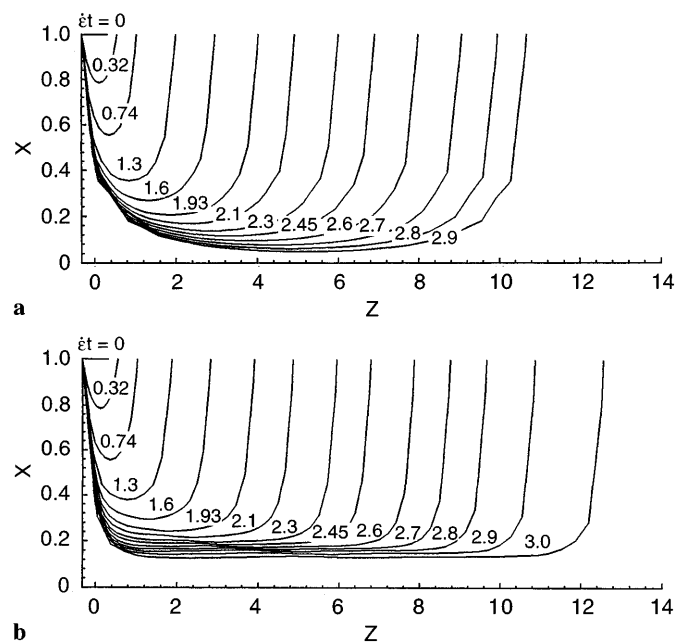
Fig. 6. Evolution of the liquid bridge interface; $\mathscr{C} = 4.7$, $\lambda = 2.0 \times 10^6$, $\Lambda_0 = 0.3143$ and $\mathscr{B} = 0$. **a** Newtonian fluid, $\mathscr{D} = 0$ **b** Oldroyd-B model $\mathscr{D} = 6$, $\beta_p = 0.28$

Sridhar (1993); Spiegelberg, Ables and McKinley (1996)). We note that only the node points of the interface have been plotted in Fig. 6 and that the apparent cusps in this figure do not exist in the calculations since the interface is represented by a cubic spline interpolant at all time steps.

For the purpose of comparison, we have obtained (from the stretching experiment by Spiegelberg, Ables and McKinley (1996)) the experimentally measured evolution of the mid-point radius, R_{mid}, of the fluid thread at an extension rate of $\dot{E} = 1.72\,\mathrm{s}^{-1}$. These measurements were made using a digital video imaging system. In Fig. 7a, the numerically predicted evolution of the liquid bridge mid-point radius, for different values of the Deborah number $\mathscr{D}$, are plotted against Hencky strain. The agreement between the simulations and the experiment is excellent up to a strain of $\dot{E}t = 2.6$. Beyond this point the numerical results predict that the radial profile decreases at a slightly faster rate than is observed in the experiment suggesting that the Oldroyd-B model does not provide enough strain hardening (or stress growth) to fully reproduce the experimental measurements. The slope of the curves in Fig. 7a are not constant as was the case in Fig. 5 for an ideal shear-free flow. Fig. 7b shows that the effective strain rate $\dot{\varepsilon}_{eff} = -(2/X)(dX/dt)$, computed in the middle of the fluid column, is initially higher than the imposed axial strain rate $\dot{E}$ before it rapidly drops below the imposed value at intermediate strains $\dot{E}t > 1.5$. The effective strain rate only approaches the ideal uniaxial elongation rate for strains $\dot{E}t \geq 1.5$. The effective strain rate in Fig. 7b initially evolves to a relatively constant value $\dot{\varepsilon}_{eff} \sim 3\dot{E}/2$ at low strains and this has implications for the velocity compensation technique which will be discussed later. In the case of a Newtonian fluid filament ($\mathscr{D} = 0$) capillary effects at higher strains result in an increasingly rapid rate of thinning in the mid-point region. However, for the values of $\mathscr{C}$ typical in the experiments ($\mathscr{C} > 1$) viscous stresses on the interface dominate the surface tension contribution and delay the onset of capillary break-up until very large strains. In the case of non-Newtonian filaments the rapidly growing elastic stresses dominate the interfacial force and surface tension is unimportant except very close to the end plates.

Experimental measurements of the applied force on the stationary end plate, are also compared with our numerical results. In Fig. 8, the dimensionless applied force on the stationary end plate (denoted by $\mathscr{F}_L$ in Fig. 2) is plotted against Hencky strain for the same four values of $\mathscr{D}$ presented in Fig. 7. The curves in Fig. 8 also indicate that the single mode Oldroyd equation fails to provide enough stress growth, at higher strains, to quantitatively simulate the rapidly increasing tensile force in the elongating fluid filament. The single mode model with a value of $\mathscr{D} = 6$ provides the best qualitative and quantitative agreement with the experimental force measurement up to a strain of $\dot{E}t = 2.6$ beyond which point the results diverge. We note that the $\mathscr{D} = 0$ simulation also falls directly on top of the experimental data points for values of axial strain up to $\dot{E}t = 1.2$ but the applied force for this case (Newtonian fluid) then evolves to zero as the radius of the filament continues to decrease. A clear distinction in behavior, between the values $\mathscr{D} = 1$ and $\mathscr{D} = 3$, can also be observed upon closer inspection of Fig. 8. The applied force, for the
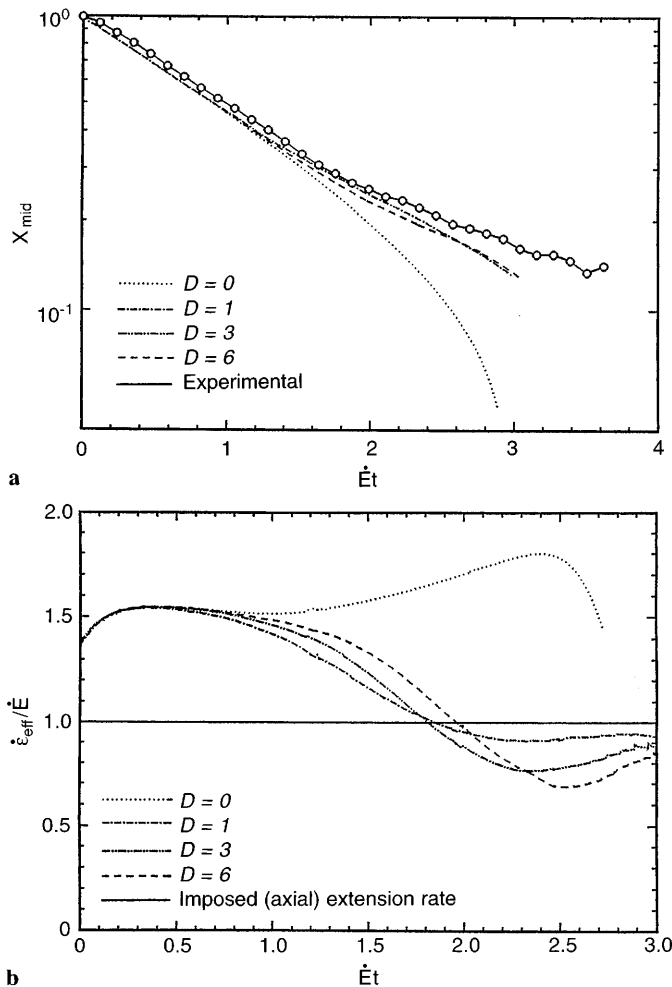

Fig. 7. Evolution of **a** the mid-point radius **b** the effective strain rate at the liquid bridge mid-point; $\mathscr{C} = 4.7$, $\lambda = 2.0 \times 10^6$, $\Lambda_0 = 0.3143$, $\beta_p = 0.28$ and $\mathscr{B} = 0$
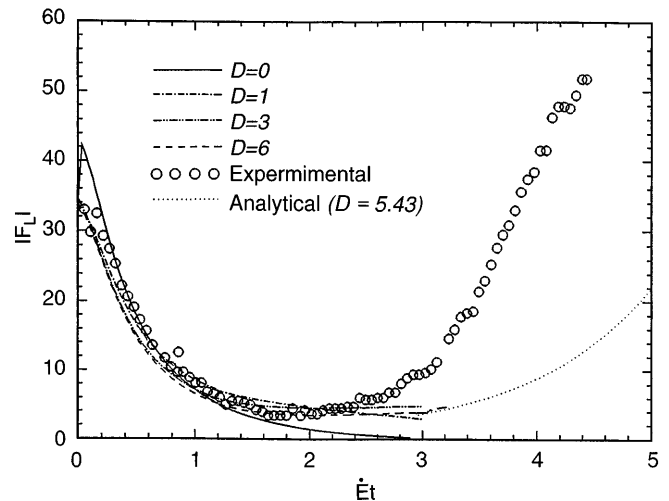
Fig. 8. Evolution of the absolute value of the applied force on the stationary end plate; Oldroyd-B model; $\mathscr{C} = 4.7$, $\lambda = 2.0 \times 10^6$, $\Lambda_0 = 0.3143$, $\beta_p = 0.28$ and $\mathscr{B} = 0$

case $\mathscr{D} = 1$, does not plateau (at least up to $\dot{E}t = 3.0$) and appears to be slowly evolving to zero whereas the force, in the case $\mathscr{D} = 3$, levels off at $\dot{E}t \approx 2$ and subsequently begins increasing. The critical value separating these two classes of behavior is $\mathscr{D} = 1$ in the case of an ideal extensional flow at an extension rate of $\dot{\varepsilon}_{\text{eff}} \equiv \dot{E}_0$ and, arises since at large strains the stresses grow exponentially with time as $\tau_{zz} \sim \exp((2 - 1/\mathscr{D})\dot{E}_0 t)$ while the filament radius decreases with time as $R_{\text{mid}} \sim \exp(-1/2\dot{E}_0 t)$ leading to an evolution of the force $F_L \sim \exp((1 - 1/\mathscr{D})\dot{E}_0 t)$, which becomes constant when $\mathscr{D} = 1$ (Harlen (1995)). In the calculation, the computed or effective strain rate for fluid elements near midplane is in fact $\dot{\varepsilon}_{\text{eff}}/\dot{E} < 1$ (cf Fig. 7b) so the force $\mathscr{F}_L$ in fact decreases weakly with strain. The dotted curve in Fig. 8 represents the projected stress growth using the analytical prediction for an ideal extensional flow of the Oldroyd-B model (14), at large strains and at an effective strain rate $\dot{\varepsilon}_{\text{eff}} = 0.9\dot{E}$, subject to the initial stress $\tau_{zz}^{(0)}$ which is taken to be the numerically computed stress at $\dot{E}t = 3$. The value $\dot{\varepsilon}_{\text{eff}} = 0.9\dot{E}$ was estimated from Fig. 7b and used as the effective strain rate that is approached in the simulations at $\dot{E}t > 3$. The corresponding Deborah number is then $\mathscr{D} = 5.43$. The numerical simulation for the case $\mathscr{D} = 6$ was continued to a strain of $\dot{E}t = 3.4$ to verify the good agreement with the analytical curve which was started at $\dot{E}t = 3$.

We now proceed to justify why an analytic one-dimensional expression is sufficient to describe the force evolution (and hence the Trouton ratio) for strains of $\dot{E}t = 3$ and higher. It is already apparent from Fig. 6 that a cylindrical region forms in the middle of the fluid sample where sample deformation occurs at a nearly constant strain rate. Contour plots for the evolution of the tensile stress are presented in Figures 9 and 10. Figure 9 shows the evolution of the total tensile stress $\mathbf{T}_{zz}^N$ for a purely viscous fluid column (Newtonian fluid). The contours in this figure show that the radial distribution of $\mathbf{T}_{zz}^N$ in the middle region of the fluid column is non-uniform for low strains. Since $\mathbf{T}_{zz}^N$ has been non-dimensionalized with a characteristic viscous stress $\eta_0 \dot{E}$, the contours essentially represent local values of an effective Trouton ratio (scaled on the nominal axial elongation rate, rather than the effective strain rate actually experienced by fluid elements near the mid point of the column). At large strains, the tensile stress $\mathbf{T}_{zz}^N$ in the column becomes increasingly radially uniform. The largest values are obtained in the narrowest region of the fluid filament near the midpoint $X_{\text{mid}}(t)$ and the regions near the rigid end plates are quiescent with almost no viscous tensile stress. Since the response of a non-Newtonian liquid bridge described by the Oldroyd-B model is initially the same as that of a Newtonian fluid at small strains, the same axial and radial nonuniformities in the non-Newtonian tensile stress τ_{zz} can be observed in Fig. 10 for the case $\mathscr{D} = 6$ with the important difference that the non-Newtonian tensile stresses remain axially and radially non-uniform even at high strains. This radial nonhomogeneity in the stress is a result of the nonhomogeneous flow in the fluid column at short times (small strains) and is "remembered" by the elastic fluid even at higher strains. The radial distribution of the normalized axial stress $\tau_{zz}/(\tau_{zz})_{\text{int}}$ is shown in

Fig. 11 as a function of the rescaled radial coordinate x/X_{mid}, where X_{mid} is the instantaneous dimensionless radius in the middle of the liquid bridge, and $(\tau_{zz})_{\text{int}}$ is the tensile stress on the fluid interface at X_{mid}. It can be seen from Fig. 11 that the tensile stresses near the midplane of the filament evolve in a self similar manner for axial strains of $\dot{E}t \geq 2.3$. Knowledge of the evolution of the fluid particle on the interface (in the middle of the fluid column) is thus sufficient to completely reproduce the self similar stress profile at higher strains. In a sufficiently strong stretching flow, i.e. $\mathscr{D} > 1/2$, it can be seen from equation (31) that the initial stress boundary condition $\tau_{zz}^{(0)}$ is not forgotten even though the Oldroyd-B model is conventionally thought of as a fluid with "fading memory". The spatial variations in τ_{zz} throughout the liquid column thus become "frozen" into the fluid as the filament is elongated and are convected with fluid elements without decaying. The stress profile shown in Fig. 11 can be integrated radially to obtain the dimensionless applied force according to

$$\mathscr{F}_L(t) = 2\pi \int_0^{X_{\text{mid}}(t)} \tau_{zz}(x, t)x\,\mathrm{d}x + \pi\frac{X_{\text{mid}}^2}{\Lambda_0} - \pi\frac{X_{\text{mid}}}{\mathscr{C}} \;,$$

$$(32)$$

where the second term represents viscous contributions from the solvent and the third term represents capillary pressure contributions. We note that at high strains (and high tensile stresses) the viscous solvent and capillary pressure contributions are negligible. Expressions (24) and (25) can be used to obtain values for the corresponding Trouton ratios.

We now turn to a discussion of the applicability of the various Trouton ratio expressions presented in Section 2. We first present in Fig. 12 the Trouton ratio values given by expressions (23–25), for the case $\mathscr{D} = 0$, compared to the well known and expected analytical result for a Newtonian fluid, $\text{Tr} = 3$. The effective Trouton ratio Tr_{point} based on a point-wise measure of the stress and local extension rate reproduces the analytical result almost exactly up to a strain of $\dot{E}t = 2.2$ before the fluid column starts to undergo capillary breakup and additional shearing and extensional effects become important in the middle of the filament (where the stresses are calculated and used in equation (25)).

Of the remaining estimates for the Trouton ratio, it is clear that equation (24) which takes into account the capillary pressure variation and the variation in the effective strain rate $\dot{\varepsilon}_{\text{eff}}$ with time provides the best estimate of the Trouton ratio actually obtained in a filament stretching rheometer. Also in Fig. 12, the Trouton ratio expression Tr_{eff} levels off to a value $\text{Tr}_{\text{eff}} = 3.5$. This slight difference from the analytical result can be rationalized by the fact that Tr_{eff} represents a mean value for the Trouton ratio and that our numerical results show the shearing effects on or near the interface are two orders of magnitude larger than along the symmetry plane ($x = 0$) of the liquid bridge. Interfacial tension and an increasing curvature are responsible for this effect and contribute to this increase in the calculated Trouton ratio value. These shearing effects are clearly not present in the analytical

Fig. 9. Evolution of the tensile stress; $\mathcal{D} = 0$, $\mathcal{C} = 4.7$, $\lambda = 2.0 \times 10^6$, $\Lambda_0 = 0.3143$ and $\mathcal{B} = 0$. (a) $\dot{E}t = 0.2$ (b) $\dot{E}t = 1.2$ (c) $\dot{E}t = 2$ (d) $\dot{E}t = 2.8$. The contour scale for the dimensionless axial stress is the same in (a), (b), (c) and (d) ▶
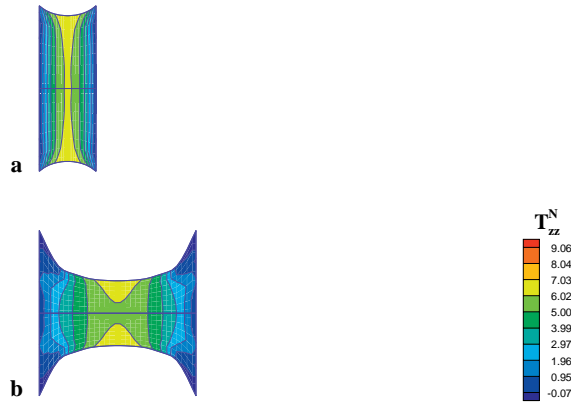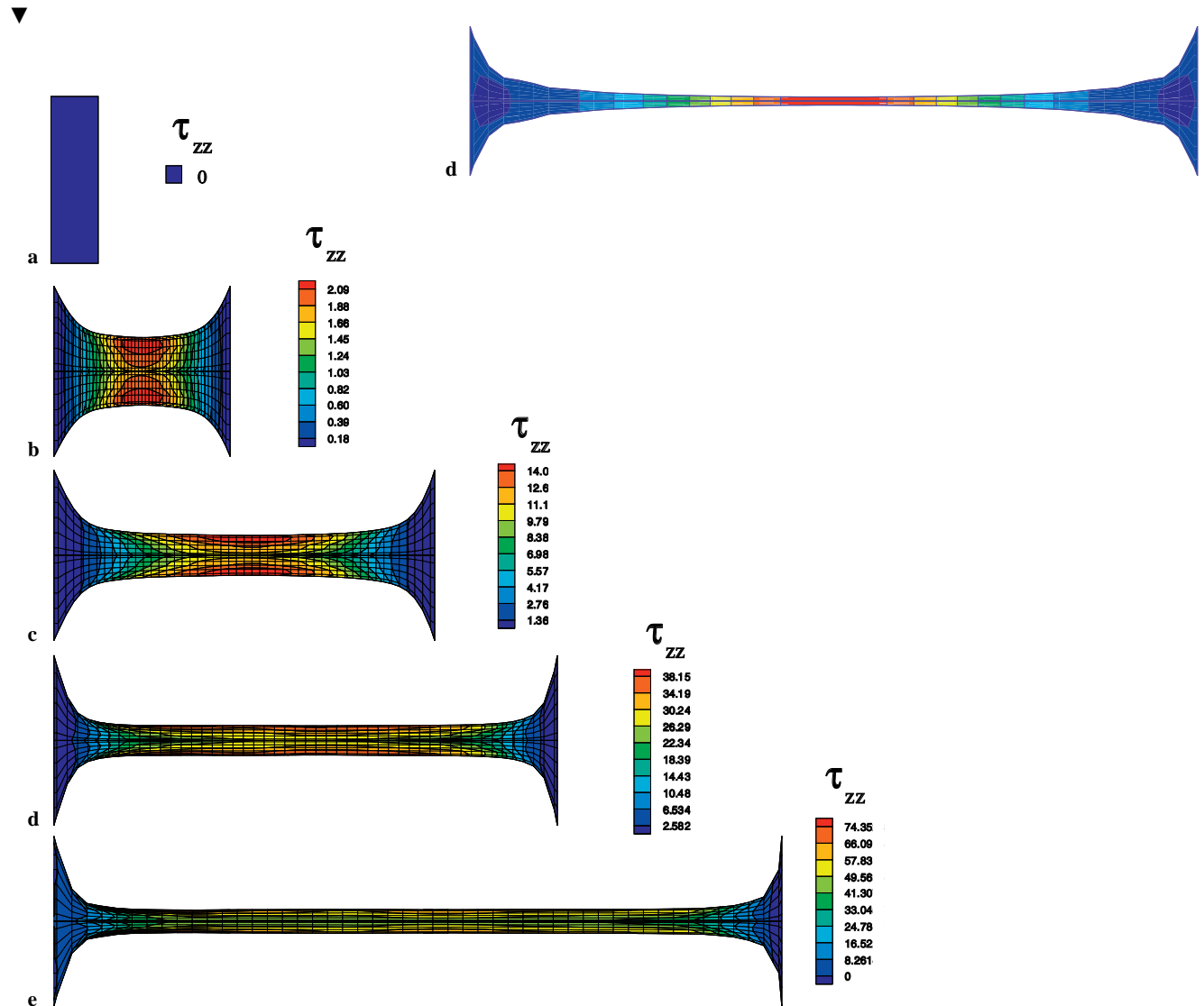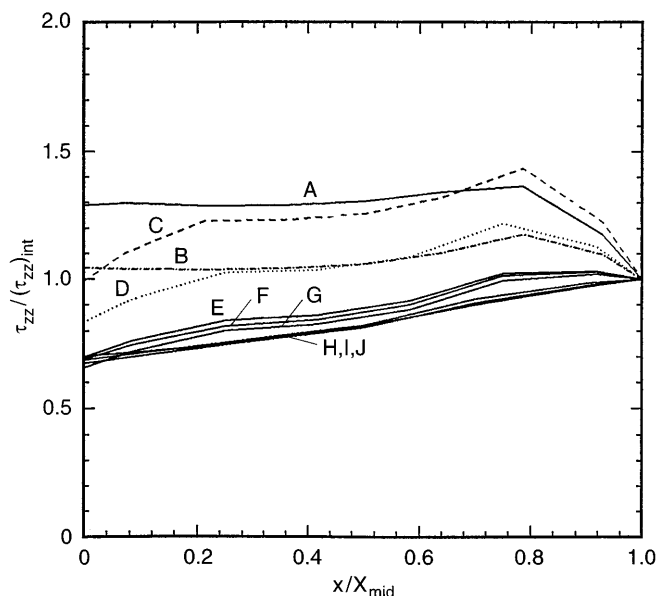
472

Fig. 10. Evolution of the tensile stresses; $\mathcal{D} = 6$, $\mathcal{C} = 4.7$, $\lambda = 2.0 \times 10^6$, $\Lambda_0 = 0.3143$ and $\mathcal{B} = 0$. (a) $\dot{E}t = 0$ (b) $\dot{E}t = 1.2$ (c) $\dot{E}t = 2$ (d) $\dot{E}t = 2.5$ (e) $\dot{E}t = 3$ ▼

Curve	$\dot{E}t$	X_{mid}	$(\tau_{zz})_{int}$
A	0.45	0.71	0.16
B	0.85	0.52	0.74
C	1.00	0.46	0.97
D	1.20	0.40	1.98
E	1.53	0.31	5.78
F	1.75	0.27	9.80
G	1.96	0.23	15.10
H	2.30	0.19	27.52
I	2.75	0.16	48.95
J	2.96	0.14	65.50

Fig. 11. Radial distribution of the normalized polymeric tensile stress at the liquid filament mid-point; $\mathscr{D} = 6$, $\mathscr{C} = 4.7$, $\lambda = 2.0 \times 10^6$, $\Lambda_0 = 0.3143$ and $\mathscr{B} = 0$
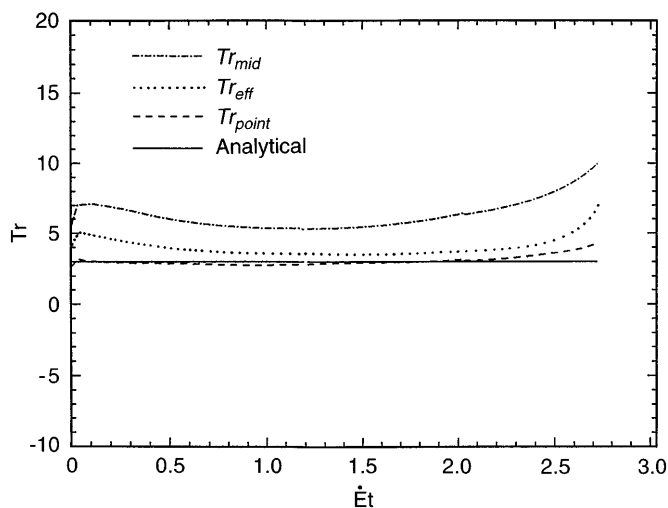

Fig. 12. Evolution of the Trouton ratio; $\mathscr{D} = 0$, $\mathscr{C} = 4.7$, $\lambda = 2.0 \times 10^6$, $\Lambda_0 = 0.3143$ and $\mathscr{B} = 0$
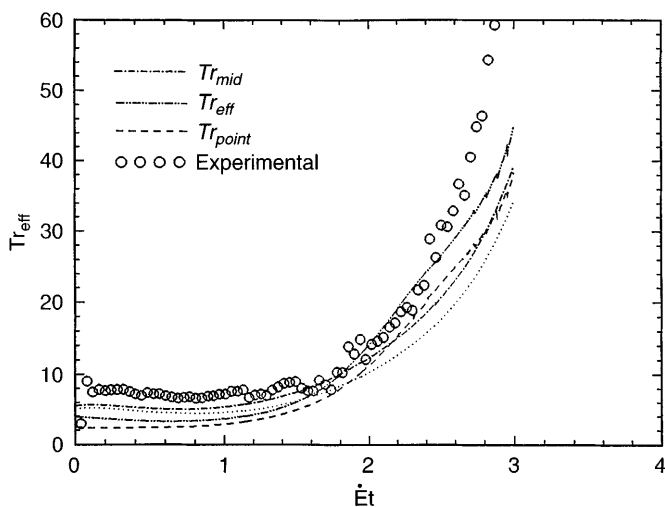

Fig. 13. Evolution of the transient Trouton ratio predicted by Oldroyd-B model and observed in experiments; $\mathscr{D} = 3$, $\mathscr{C} = 4.7$, $\lambda = 2.0 \times 10^6$, $\Lambda_0 = 0.3143$, $\beta_p = 0.28$ and $\mathscr{B} = 0$

(ideal) Trouton ratio Tr = 3. The radial stress τ_{rr} on the interface is also two to three times smaller than at the center while the tensile stress is uniform along the radial coordinate. Even though Fig. 7b shows the variation of the effective strain rate $\dot{\varepsilon}_{eff}$ with time for this case, excellent agreement with the analytical value of Tr = 3 is obtained because, for a Newtonian fluid, the strain rate history is not important. However, the evolution of the stresses in a non-Newtonian fluid filament depends upon the entire history of imposed strain rate and a varying strain rate does not provide a fundamental way in which to compute the transient Trouton ratio of an unknown fluid. Velocity compensation techniques are used experimentally (Tirtaatmadja and Sridhar (1993); Spiegelberg, Ables and McKinley (1996)) to generate a constant strain rate in the middle of the fluid thread. We will perform *numerical* velocity compensation in Section 4.2.3.

Values of Trouton ratio for the simulations presented in Figures 7–8 are shown in Fig. 13 for the case $\mathscr{D} = 3$. Expression (24) was also used to calculate Trouton ratio values using the experimental force and radius measurements and this experimental result is included in Fig. 13 for comparison. We note that the effective strain rate was not measured in the experiment since differentiation of the discretely measured $R_{mid}(t)$ data is required. Unsurprisingly, all the Trouton ratio expressions discussed in Section 2 provide the right qualitative behavior given the fact that at large strains, tensile stresses can be several orders of magnitude larger than any other stresses in the fluid. At small strains, the point-wise Trouton ratio (Tr_{point}) provides the most accurate prediction of the analytical value Tr = 3 for the essentially Newtonian response of the fluid. The difference in values for Tr_{eff} and Tr_{point} in Fig. 13 is due to the fact that Tr_{eff}, in contrast to Tr_{point} (which is a local value), represents a radially averaged value and that, as is apparent in Fig. 10, the tensile stresses vary radially in the middle region. The main result from Fig. 13 is that the Oldroyd-B constitutive equation predicts the steep rise in Trouton ratio at slightly higher strains than is observed in the experiment, which is consistent with our earlier
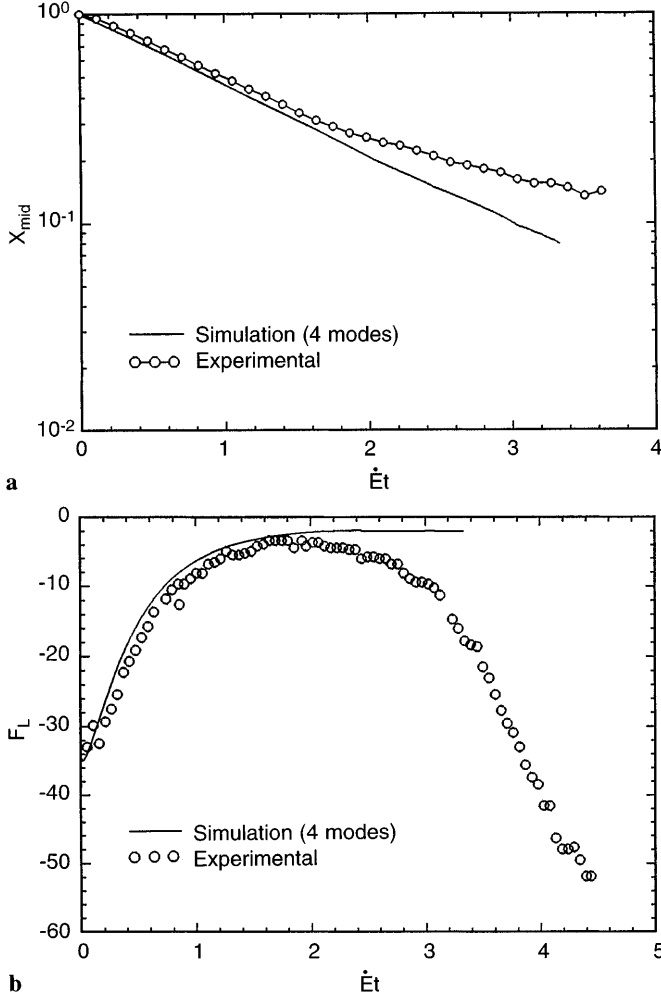
Fig. 14. Evolution of **a** the mid-point radius **b** the applied force on the stationary end plate using a four mode formulation of the Generalized Maxwell model with a Newtonian solvent; $\mathscr{C} = 4.7$, $\lambda = 2.0 \times 10^6$, $\Lambda_0 = 0.3143$ and $\mathscr{B} = 0$
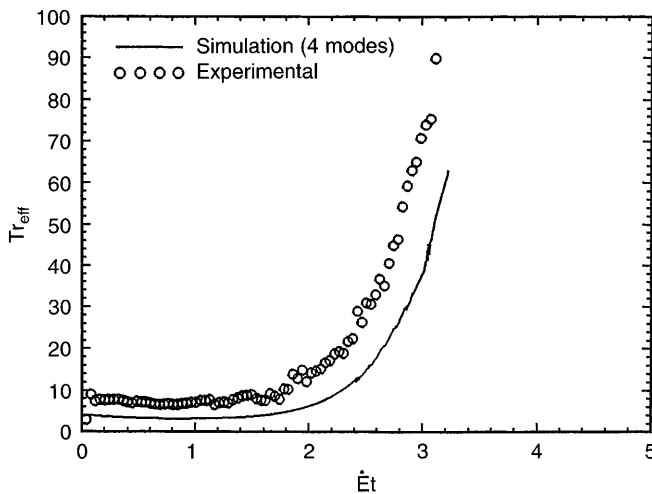

Fig. 15. Evolution of the effective Trouton ratio $\mathrm{Tr}_{\mathrm{eff}}$; $\mathscr{C} = 4.7$, $\lambda = 2.0 \times 10^6$, $\Lambda_0 = 0.3143$ and $\mathscr{B} = 0$

observation that the stress growth predicted by this quasi-linear model is not sufficient.

4.2.2
Four-mode convected Maxwell model

In this section we present results of our numerical simulations of the filament stretching device, using the four-mode convected Maxwell equation to more accurately model the viscoelastic response of the stresses in the experimental test fluid.

In Fig. 14a, the evolution of the middle radius is plotted as a function of strain and shows that, for strains of $\dot{E}t \geq 1.6$, the results diverge from the experimental measurements. The four-mode model results are initially surprising since they are less accurate than those obtained using the single-mode model. The problem, again, is the lack of stress growth at strains of $\dot{E}t \geq 1.6$. Each mode in the generalized convected Maxwell model behaves as a Newtonian fluid in the limit $\mathscr{D}_i \rightarrow 0$. So adding more modes with $\lambda_i < \lambda_1$ simply pushes significant strain hardening to higher strain levels since the elastic modulus $G = \sum_i (\eta_i/\lambda_i)$ of the material is redistributed from the single-mode model to modes that have lower $\mathscr{D}_i$ and thus contribute less to the total stress. What is clearly required for increased strain hardening at moderate strains is the superposition of multiple modes of nonlinear models such as the Chilcott-Rallison and Phan-Thien-Tanner models or the incorporation of additional *dissipative* terms in the constitutive equation which result in faster stress growth than the exponential response given by equation (31) (Tirtaatmadja and Sridhar (1995); Rallison (1997)).

The applied force (Fig. 14b) and computed value of the effective Trouton ratio at the midpoint of the column (Fig. 15) results also show the same lack of strain hardening at moderate strains.

4.2.3
Velocity compensation

As we have shown above, direct calculation of the Trouton ratio is preferred using kinematic data from the middle of the fluid bridge were shearing effects are minimal. However, the effective strain rate $\dot{\varepsilon}_{\mathrm{eff}}$ has been shown to vary temporally in this region. We now emulate the experimental attempts that are made to compensate for this strain rate variation (Tirtaatmadja and Sridhar (1993); Spiegelberg, Ables and McKinley (1996)) and implement a numerical procedure that generates constant effective strain rates in the middle of the filament. The only modification that is required to the algorithm presented in Section 3.4 is that at steps (i) and (ii), an iterative procedure is established whereby different velocity boundary conditions on the moving plate are imposed until the strain rate in the middle converges to the desired constant value. A shooting method is used to insure convergence. All the other steps in the algorithm are followed as before.

In Figures 16 and 17, we show the results obtained with the single-mode Oldroyd-B equations with $\mathscr{D} = 3$. Figure 16 shows the evolution of the dimensionless imposed velocity on the right end plate and is plotted versus the effective Hencky strain $\varepsilon = \int \dot{\varepsilon}_{\mathrm{eff}}(t)\, \mathrm{d}t$. The iterative procedure performs well in generating a constant strain rate at

the filament midpoint. The only reported experimental practice (Spiegelberg, Ables and McKinley (1996)) for insuring a constant rate in the experiments is to apply a velocity profile composed of two exponentially varying elements, at two distinct stretch rates, with a smooth transition region between the two. This approach yields relatively constant rates. Figure 16, plotted on a semilogarithmic scale, suggests that the correct velocity profile is more complicated than a single or double exponential profile and only asymptotically approaches the ideal uniaxial extensional profile at strains $\varepsilon > 3.5$.

The attempts to generate a constant strain rate are made to provide more accurate calculations (or measurements) of the Trouton ratio. We thus verify in Fig. 17 that the Trouton ratio calculations, for the simulations using the velocity compensation technique, provide excellent agreement with the analytical result for the Trouton ratio
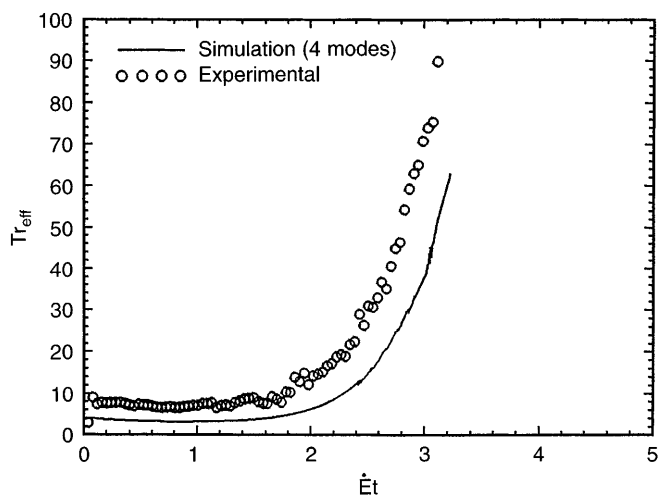

Fig. 16. Evolution of the imposed dimensionless velocity on the right end plate and the effective dimensionless strain rate in the middle of the fluid filament; $\mathscr{D} = 3$, $\mathscr{C} = 4.7$, $\lambda = 2.0 \times 10^6$, $\Lambda_0 = 0.3143$ and $\mathscr{B} = 0$
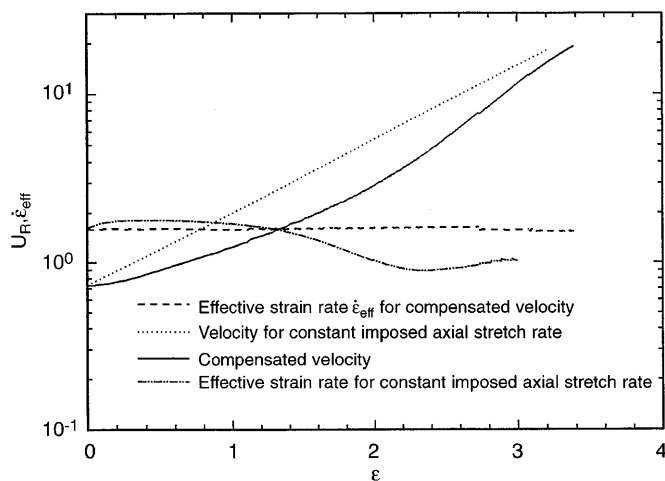

Fig. 17. Evolution of the Trouton ratio; $\mathscr{D} = 3$, $\mathscr{C} = 4.7$, $\lambda = 2.0 \times 10^6$, $\Lambda_0 = 0.3143$ and $\mathscr{B} = 0$

of a liquid filament evolving in a shear-free flow at the corresponding effective strain rate.

5
Conclusions

In this paper, we have presented the results of numerical simulations of the filament stretching devices used by Sridhar, Tirtaatmadja, Nguyen and Gupta (1991), Tirtaatmadja and Sridhar (1993) and Spiegelberg, Ables and McKinley (1996). The boundary element method was used to simulate the extensional dynamics of extending Newtonian and non-Newtonian fluid bridges, and, the Oldroyd-B (single mode) and the generalized Maxwell model (four modes) were used to model the stresses in the liquid filament. Parameters for the numerical calculations were chosen to match an experiment conducted by Spiegelberg, Ables and McKinley (1996) and direct comparisons with these experimental results were made. Results show that the Oldroyd-B constitutive equation fails to adequately model the high stress growth observed experimentally at strains of $\dot{E}t \geq 2.4$ although excellent agreement is obtained at lower values of strain. In fact, significant strain hardening with the single mode model occurs at higher strains than in the experiment (see Fig. 8). The four-mode convected Maxwell model only provides significant strain hardening at yet higher strains due to the lowered elasticity of the dominant relaxation mode. It was also found that for strains of $\dot{E}t \geq 2.3$, the tensile stresses in the middle region of the liquid filament evolve in a self similar manner. Since the effective strain rate $\dot{\varepsilon}_{eff}$ in the middle of the liquid column was also shown to approach a relatively constant value, we have shown in Section 4.2.1 that the evolution of the mid-point radius, the applied force on the stationary end plate and the Trouton ratio, for strains $\dot{E}t \geq 2.3$, can in fact be predicted by use of the analytical expressions for an ideal extensional flow, and initial conditions for the stress obtained from numerical calculations. Qualitatively similar results are to be expected for the other nonlinear elastic models that show pronounced strain hardening (e.g. FENE dumbell models). However, the quantitative evolution of such liquid filaments will of course depend on the initial conditions obtained from the numerical calculation.

The ultimate goal of a filament stretching device is to make unambiguous measurements of the transient tensile stress growth in a viscoelastic fluid which can be quantitatively compared with the prediction obtained from appropriate constitutive models in ideal uniaxial elongation. To this end, different expressions for calculating the Trouton ratio from the actual dynamical response of the bridge were also compared in order to highlight the advantages and disadvantages of each. A point-wise expression, Tr_{point} (25), which uses local stress values and an effective strain rate calculated in the middle of the liquid filament, exactly reproduces the analytical result $Tr = 3$ for a Newtonian fluid and provides the most accurate Trouton ratio values in general. Velocity compensation techniques (numerical and experimental) assure a constant effective strain rate at the liquid bridge mid-point and render this expression even more accurate. However, point-wise measurement of stresses, which rely on bire-

fringence techniques, are difficult to achieve experimentally so that a Trouton ratio which utilizes the measured force on the stationary end plate is usually employed in experimental analyses. The Trouton ratio expression (24), based on a force balance containing half of the liquid bridge, uses the measured applied force and information from the filament mid-point where the flow is nearly shear-free and provides an adequate, but not perfect, way (compared to Tr_{point}) of computing the Trouton ratio. The disadvantage of Tr_{eff} is the fact that it represents a radially averaged value of the stress in the fluid filament which is significant because of the pronounced non-uniform radial variation in the tensile stress. This distribution arises as a result of the initial shear flow in the fluid near the rigid end plates, and clearly care has to be taken in experimental design of such devices. Other approximate expressions for the Trouton ratio based on force balances on the stationary end plate and/or the applied strain rate yield results which still contain shearing effects and are therefore undesirable. We thus conclude that until point-wise measurements of stress are experimentally feasible, precise measurements of the uniaxial stress growth in an ideal uniaxial elongational flow are difficult to achieve using the filament stretching device unless great care is taken in experimental selection of the initial aspect ratio and velocity compensation profile. The transient extensional viscosities that are measured using these devices even without such corrective techniques are however a clear advance on other experimental techniques to date and, are probably very adequate and useful quantities to be employed in most practical, engineering situations.

References

Berg S, Kröger R, Rath HJ (1994) Measurement of extensional viscosity by stretching large liquid bridges in microgravity. J. Non-Newtonian Fluid Mech. 55:307–319

Bird RB, Armstrong RC, Hassager O (1987) Dynamics of Polymeric Liquids. Fluid Mechanics vol. 1. New York: Wiley Interscience.

Burden RL, Faires JD (1985) Numerical Analysis, 3rd ed. Boston: Prindle, Weber & Schmidt

Bush MB (1984) In: Brebbia, CA (ed): Topics in Boundary Element Research, vol. 5. Berlin: Springer-Verlag

Bush MB, Milthorpe JF, Tanner RI (1984) Finite element and boundary element methods for extrusion computations. J. Non-Newtonian Fluid Mech. 16:37–51

Bush MB, Tanner RI, Phan-Thien N (1985) A boundary element investigation of extrudate swell. J. Non-Newtonian Fluid Mech. 18:143–162

Ferguson J, Hudson NE (1993) Transient elongational rheology of polymeric fluids. Eur. Polym. J. 29:141–147

Gaudet S (1996) Extensional dynamics of liquid bridges and filament stretching devices. Ph.D. Thesis, Harvard University.

Gaudet S, McKinley GH, Stone HA (1996) Extensional deformation of Newtonian liquid bridges. Phys. Fluids. 8:2568–2579

Gupta RK, Sridhar T (1988) Collyer AA, Clegg DW (ed): Rheological Measurement, pp. 211–245. London: Elsevier Applied Science.

Harlen OG (1996) Personal communication

Hermanksy CG, Boger DV (1995) Opposing-jet viscometry of fluids with viscosity approaching that of water. J. Non-Newtonian Fluid Mech. 56:1–14

James DF, Walters KA (1993) Techniques in Rheological Measurement. London: Elsevier.

Keiller RA (1992) Extending filaments of an Oldroyd fluid. J. Non-Newtonian Fluid Mech. 42:37–48

Keiller RA (1992) Modelling of the extensional flow of the M1 fluid with the Oldroyd equation. J. Non-Newtonian Fluid Mech. 42:49–64

Khagram M, Gupta RK, Sridhar T (1985) Extensional flow of xanthan gum solutions. J. Rheol. 29:191–207

Kreyszig E (1993) Advanced Engineering Mathematics, 7th ed. New York: John Wiley & Sons.

Lucas SK (1995) Some developments of the boundary integral equation method, and applications in free surface and elasticity problems. Ph.D. Thesis, University of Sydney.

Meissner J (1985) Chem. Eng. Commun. 33:159–180

Meissner J (1985) Rheometry of polymer melts. Ann. Rev. Fluid Mech. 17:45–64

Pozrikidis C (1992) Boundary Integral and Singularity Methods for Linearized Viscous Flow. Cambridge University Press.

Rallison JM (1997) Dissipative stresses in dilute polymer solutions. J. Non-Newtonian Fluid Mech. 68:61–83

Rallison JM, Acrivos A (1978) A numerical study of the deformation and burst of a viscous drop in an extensional flow. J. Fluid Mech. 89:191

Shipman RWG, Denn MM, Keunings R (1991) Mechanics of the "falling plate" extensional rheometer. J. Non-Newtonian Fluid Mech. 40:281–288

Spiegelberg SH, Ables DC, McKinley GH (1996) The role of end-effects on measurements of extensional viscosity in viscoelastic polymer solutions with a filament stretching rheometer. J. Non-Newtonian Fluid Mech. 64 (2–3), 229–267

Sridhar T, Tirtaatmadja V, Nguyen DA, Gupta RK (1991) Measurement of extensional viscosity of polymer solutions. J. Non-Newtonian Fluid Mech. 40:271–280

Tanzosh J, Manga M, Stone HA (1992) Boundary integral methods for viscous free-boundary problems: Deformation of single and multiple fluid-fluid interfaces. In: Proceedings of Boundary Element Technologies VII Brebbia, CA & Ingber, MS (eds): Computational Mechanics Publications, 19

Tirtaatmadja V, Sridhar T (1995) Comparison of constitutive equations for polymer solutions in uniaxial extension. J. Rheol. 39:1081–1160

Tirtaatmadja V, Sridhar T (1993) J. Rheol. 37:1081

Toose EM, Geurts BJ, Kuerten JGM (1995) A boundary integral method for two-dimensional (non)-Newtonian drops in slow viscous flow. J. Non-Newtonian Fluid Mech. 60:129–154

Trouton FT (1906) On the coefficient of viscous traction and its relation to that of viscosity. Proc. Roy. Soc. A. 77:426

Zheng R, Phan-Thien N (1992) A boundary element simulation of the unsteady motion of a sphere in a cylindrical tube containing a viscoelastic fluid. Rheologica Acta. 31:323–332